Synergistic Storage of Lithium Ions in Defective Anatase/Rutile TiO_2 for High-rate Batteries

*Weixin Song[a], Qianfan Jiang[a], Xiangyu Xie[a], Adam Brookfield,[b] Eric J. L. McInnes[b], Paul R. Shearing[c], Dan J.L. Brett[c], Fang Xie[a], D. Jason Riley[a]**

E-mail: Jason.riley@imperial.ac.uk

[a] *Department of Materials and London Centre for Nanotechnology, Imperial College London, London, UK.*

[b] *EPSRC National EPR Facility, School of Chemistry and Photon Science Institute, The University of Manchester, Manchester, UK.*

[c] *Electrochemical Innovation Lab, Department of Chemical Engineering, University College London, London, UK.*

Synergistic Storage of Lithium Ions in Defective Anatase/Rutile TiO_2 for High-rate Batteries

Abstract

Fabrication of heterostructured materials is a strategy to boost the charge-transfer kinetics and the performance of high-rate lithium storage. Here, a facile, low-temperature method for the synthesis of high-area TiO_2 nanospheres containing both anatase and rutile phases is described. The as-prepared materials contain a high concentration of oxygen vacancies facilitating electron conduction in the anatase phase and theoretical calculations provide evidence of a low energy barrier for Li^+ transport in the rutile phase. The synergy between the two phases renders the shared conduction of electrons through anatase and Li^+ ions *via* rutile at high-current rates, leading to the anodes that outperform the alternate TiO_2 systems when the combination of capacity at high current densities and cycle stability are considered, displaying a capacity of 95.4 mAh g^{-1} at 10 A g^{-1} and a 97.2 % retention of capacity over 500 cycles at 1 A g^{-1}.

Keywords: anatase and rutile TiO_2; oxygen vacancy; lithium storage; synergistic effect

Introduction

Titanium dioxide (TiO_2), also known as titania, has been widely studied as an anode material in rechargeable batteries and as a photocatalyst for solar-cell devices, water splitting and air purification[1]. TiO_2 of different polymorphs have been considered as promising anode materials owing to their low cost[2], non-toxicity, high stability, low volume expansion upon lithiation[3] and improved safety[4]. Graphite, the most common anode in commercial cells, suffers extreme expansion (~150%) when solvated intercalation occurs, leading to a deconstructed graphite structure and poor storage capability[5]. In contrast, the polymorphs of anatase, rutile and TiO_2-B (bronze) have excellent phase stability on repeated lithiation/delithiation, owing to the facile accommodation of lithium ions in the crystal structures. The theoretical capacities of TiO_2 are reported as 168 mAh g^{-1} for anatase[6] and 335 mAh g^{-1} for both rutile[7] and TiO_2-B[8] corresponding to 0.5 and 1 mol lithium insertion per mol of TiO_2, respectively. However, the achieved value is highly dependent on the particle size and a decrease in the size of anatase to nano-scale can enhance the lithium insertion to approximately 1 Li per mol of TiO_2[6]. In addition, low-dimensional nanostructures of TiO_2, including nanoparticles[9], nanotubes[10], nanowires[11], nanorod[12], nanoribbons[13] and nanosheets[14, 15] have short paths for electron and ion transport and lead to improved specific capacities as well as high-rate performance.

Both nanoscale anatase and rutile TiO_2 have been widely employed as lithium anode materials and have exhibited a wide range of results. Computational studies have shown that the three–dimensional structure of the phases means that the incorporation of Li^+ from the electrolyte is more energetically favoured for anatase than rutile[16]. In contrast, the mobility of Li^+ in rutile, especially along the c-axis, is much higher than that in anatase[17]. The possibility of using mixed anatase/rutile nanoparticles as an anode material to exploit the

advantageous properties of each phase, as observed for P25 as a photocatalyst, has not been considered in lithium storage.

The phase boundaries between anatase TiO_2 and TiO_2-B are easily formed by annealing TiO_2-B, a metastable phase of anatase[18] and engaging the crystallographic planes from both crystals to form (001)TB/(100)TA, (200)TB/(002)TA, and (020)TB/(020)TA (TB means TiO_2-B while TA is anatase TiO_2) interfaces[18-20]. The coherent interface can contribute extra lithium storage sites by the charge separation where anatase acts as the electron-accepting phase[21] while TiO_2-B is a Li^+-accepting phase, leading to enhanced capacity for lithium storage[14, 15]. The interfacial charge storage results in a large pseudocapacitance, which is beneficial for improving the high-rate capability[15]. It has been difficult to understand the interface between anatase and rutile because of the controversy surrounding the energetic alignment of the band edges and role of the interface in separating the photoexcited charge carriers[22]. However, the interfacial charge storage for Li^+ ions and electrons in a mixed-phase anatase/rutile has not been studied and the possible synergistic effect arising from both phases is also unclear.

In this work, high-surface-area TiO_2 composed of nanotubes of mixed anatase and rutile phases was synthesized from a low-temperature hydrothermal reaction and calcination. Electrochemical characterization showed that the material has a specific capacity of 167 mAh g^{-1} at 1 A g^{-1} (6C, assuming 1C is 168 mA g^{-1}) and 95 mAh g^{-1} at 10 A g^{-1} (60C). The high-rate performance is competitive compared with the previous published results, attributed to the benefits of the nanostructure and synergy of the anatase/rutile as well as the interfacial charge storage.

Results and discussion

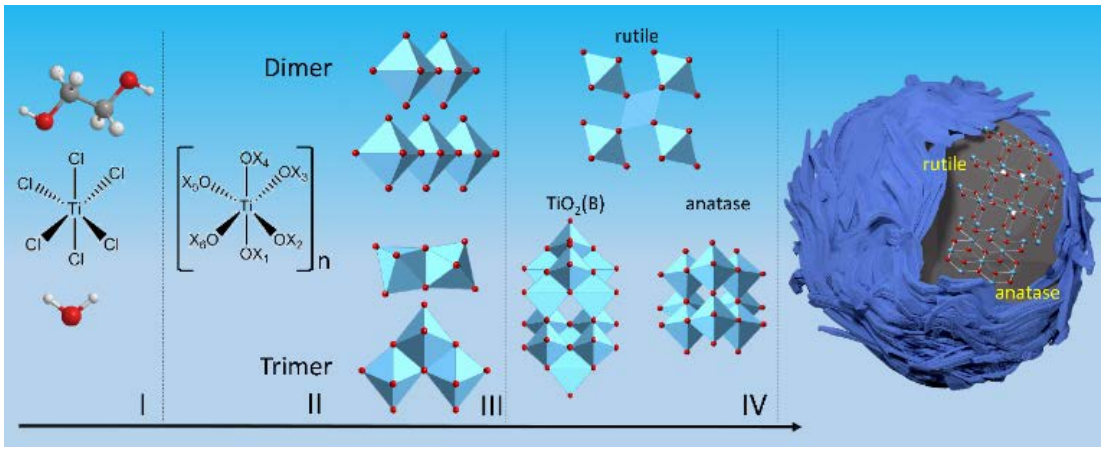

Figure 1 Nucleation growth of hydrated titanium octahedra to form TiO_2 polymorphs. (I) Molecule hydrolysis, (II) dendrimer formation, (III) nucleation growth under hydrothermal condition, (IV) crystal growth under calcination. (III) shows the short-range octahedral unit in linear packing (rutile structure) and zigzag packing (anatase structure). (IV) Shows the crystal structure of rutile, TiO_2-B and anatase. Bottom is the conversion from TiO_2-B to anatase. Right is the schematic representation of the prepared TiO_2 sphere with phase boundaries between anatase and rutile.

Figure 1 is a schematic representation of the synthesis of the anatase/rutile structure at low temperature: (I) hydrolysis, (II) dendrimer formation, (III) nucleation and (IV) crystal growth. The hydrolysis of $TiCl_3$ in ethylene glycol in the presence of a small amount of water produces the aqueous Ti-OX complex (X = H, Cl or ethyl chain)[4, 23-25]. The number and category of X are dependent on the solution pH and water concentration[23, 26]. The hydrated Ti-OX complex is a dendrimer and consists of dimers and trimers which are composed of two or three corner-linked octahedral, respectively[23]. The dendrimers are the precursors of the crystal nuclei which undergo condensation in the autoclaving step[24, 27]. The short-range crystal nuclei have phase differences resulting from the order of the Ti-O octahedral units[28, 29]. The linear packing of octahedra uses *trans*-coordination to allow one octahedron in contact with ten neighbour octahedra (two sharing edge oxygen pairs and eight sharing corner oxygen

atoms), while the zigzag packing uses *cis*-coordination results in each octahedron linking eight neighbours, in which four share edges and four share corners. The linear packing structure (rutile) has lower Gibbs free energy[30] but is unstable under kinetic control[29]. The zigzag structure is kinetically favourable because of the high ratio of *cis*-coordination sites and the probability of cis-polymization[31]. Rapid crystallization leads to the zigzag structure because of the lower surface free energy[30]. However, the linear array (rutile structure) tends to be stable when the process occurs under thermodynamic control.

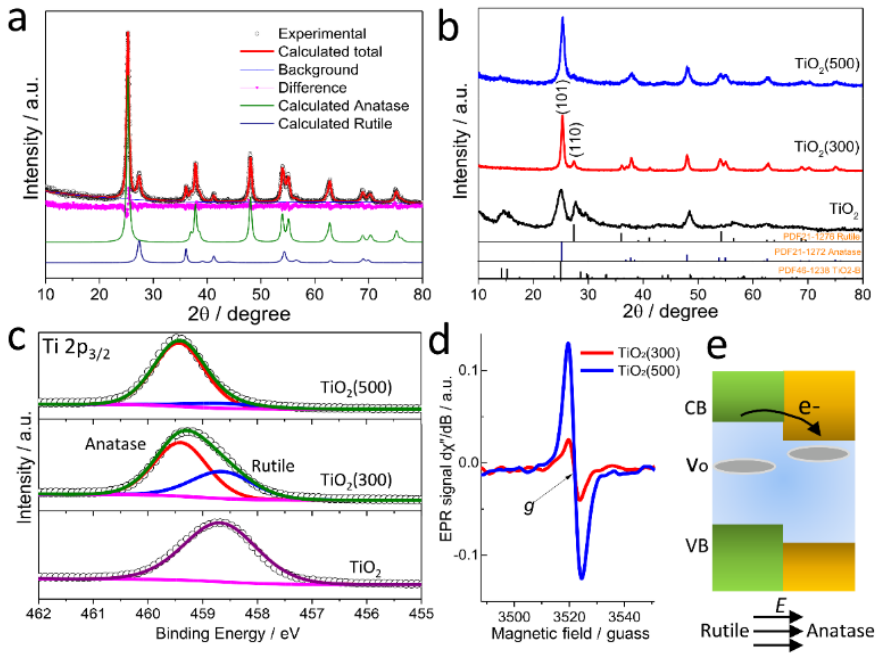

Figure 2 Characterization of the as-prepared TiO_2, TiO_2(300) and TiO_2(500). (a) XRD patterns. The labelled lattice planes, (101) and (110) in TiO_2(300) are typical for anatase and rutile phase, respectively. (b) Rietveld refinement of the XRD pattern of TiO_2(300). (c) High-resolution XPS of Ti 2p. Red and blue peaks denote anatase and rutile. Purple peak is due to the complex product. (d) X-band EPR spectra of TiO_2(300) and TiO_2(500) at room temperature. (e) Conduction band (CB) and valance band (VB) energy diagram of rutile and anatase TiO_2 with oxygen vacancies (Vo) and the built-in electric field along the interface.

The feature at 14.5° in the XRD patterns in Figure 2a indicate the as-prepared TiO_2 sample after hydrothermal reaction at 150 °C for 24 h, contains monoclinic TiO_2-B which is a metastable phase of TiO_2. The high background along the XRD pattern indicates the existence of an amorphous TiO_2 phase. The hydrothermal product is easy to convert into other polymorphs by heating at 300 °C for 2h in air; this occurs through a cation displacement from the chains to the nearby octahedral sites, followed by shear of the TiO_2-B[32, 33] and octahedral rearrangement of the amorphous TiO_2[31]. The labelled lattice planes in the XRD patterns of the sample post-annealing at 300 °C, TiO_2(300), match the (101) of anatase and (110) of rutile. The (110) plane diffraction peak for TiO_2(300) indicates the rutile crystals were present in the hydrothermal TiO_2 product because the strong binding energy of Ti-O means anatase cannot transform to the rutile phase in the absence of a melting-point process[29, 30]. According to the Scherrer equation, in TiO_2(300) the crystal size of anatase along the (101) direction is 16.6 nm, and that of rutile along the (110) direction is 19.4 nm. Rietveld refinement, Figure 2b, on the XRD pattern of TiO_2(300), reveals both phases have the lattice parameters of a tetragonal crystal, Table 1. The corresponding weight ratio of anatase and rutile is 79% and 21%, similar to Degussa P25 (80 wt% anatase and 20 wt% rutile)[22, 30]. The heating of the hydrothermal product at 500 °C for 2h in air, TiO_2(500), transforms more of the amorphous phase enriching anatase. A higher calcination temperatures of 600 or 750 °C for 2h in air results in the anatase irreversibly converting into rutile and promotes crystal growth, see Figure S1 and Table S1.

Table 1 Lattice parameters and phase ratio of the mixed anatase and rutile in TiO_2(300) through Rietveld refinement.

TiO_2(300)	a	b	c	Volume ratio	Weight ratio
Anatase	3.7843(57)	3.7843(57)	9.4992(91)	80.1%	78.7%
Rutile	4.5991(74)	4.5991(74)	2.9537(05)	19.9%	21.3%

High-resolution XPS of Ti $2p_{3/2}$ in the hydrothermal TiO_2 product, TiO_2(300) and TiO_2(500) are displayed in Figure 2c. The TiO_2-B dominated hydrothermal product shows one fitted peak at 458.7 eV, while TiO_2(300) and TiO_2(500) are fitted by two peaks assigned to anatase and rutile, which are located at 459.3 and 458.9 eV, with a 0.4 eV higher binding energy for anatase. The binding energy of Ti $2p_{3/2}$ of TiO_2-B or the amorphous TiO_2 is lower than rutile and anatase. The deconvolution of the Ti $2p_{3/2}$ spectra also provides a quantitative estimate of the atomic ratio of anatase to rutile. TiO_2(300) has 77% anatase and 23% rutile, consistent with the weight ratio from XRD refinement, and TiO_2(500) is composed of 93% anatase and 7% rutile. The thermogravimetry/differential scanning calorimetry (TGA/DSC) profiles of the hydrothermally prepared TiO_2, plotted in Figure S2 show two phase transition processes at 300 and 500 ^{o}C, as elucidated in the XRD analysis. High-temperature annealing causes crystal growth or aggregation, leading to a drop in specific surface area. The BET surface areas, determined by physical nitrogen adsorption/desorption in Figure S3, of TiO_2, TiO_2(300) and TiO_2(500) are 235, 130 and 75 $m^2\ g^{-1}$ respectively, with a decrease in the number of nanopores with increasing temperature. The specific surface areas of the prepared materials are much larger than that of commercial Degussa P25[34], 40 $m^2\ g^{-1}$. Ultraviolet-visible absorption spectra (UV-Vis) in Figure S4 of TiO_2, TiO_2(300) and TiO_2(500) reveal red-shifted absorption edges compared to anatase, rutile and Degussa P25, which may be due to the lattice distortion and defects in the nanocrystals that attenuate the light scattering[35-37]. Figure S5 depicts the Tauc plots of $(\alpha h\nu)^2$ *vs.* photon energy ($h\nu$) for TiO_2, TiO_2(300), TiO_2(500) and Degussa P25, which are derived via the Kubelka-Munk method[38, 39]. The band gaps are 3.47, 3.3, 3.28 and 3.29 eV, respectively. Electron paramagnetic resonance (EPR) was conducted to verify the presence of the defects and the EPR spectra of TiO_2(300) and TiO_2(500) are displayed Figure 2d.

Both samples show a strong EPR signal with a near isotropic *g*-factor of 2.002 for TiO_2(300) and 2.003 for TiO_2(500) indicating the existence of a significant number of oxygen vacancies (Vo)[40-43] which results from the oxygen depletion under the thermal annealing[44]. The electrons localized at the oxygen vacancies form a donor level below the conduction band of TiO_2 and even overlap the conduction band, leading to increased electron conductivity[42]. The direct measurements of the resistivity of the pure anatase, rutile and TiO_2(300) were carried out on the pressed pellets using the same amount of powder and pressure on a Hall effect instrument (see details in experimental section). The sheet resistivity values of anatase, rutile and TiO_2(300) are 1.3×10^{10} Ω square^{-1}, 2.6×10^{10} Ω square^{-1} and 2.4×10^{7} Ω square^{-1}, indicating a high electron conductivity of TiO_2(300) compared to the pure anatase and rutile. More oxygen vacancies prefer to form in the anatase than rutile[45] and form a shallow donor in anatase[46], as depicted in the Figure 2e, implying a facile electron conduction in the anatase component. Annealing of the hydrothermally-obtained TiO_2 at 500 °C, TiO_2(500), enhances the EPR signal compared to TiO_2(300) because the annealing of anatase and rutile in the air can increase the population of oxygen vacancies in both phases and adsorbed oxygen (O_2^-) in rutile[45]. The quantified electron concentration of TiO_2(500) is nearly 5 times higher than TiO_2(300) through the doubly integrating EPR spectra plotted in Figure S6. In the mixed-phase TiO_2, the interface between the rutile and anatase leads to the formation of a built-in electric field (*E*) because of the difference in the conduction band energy and the electron flow, making anatase an electron acceptor.

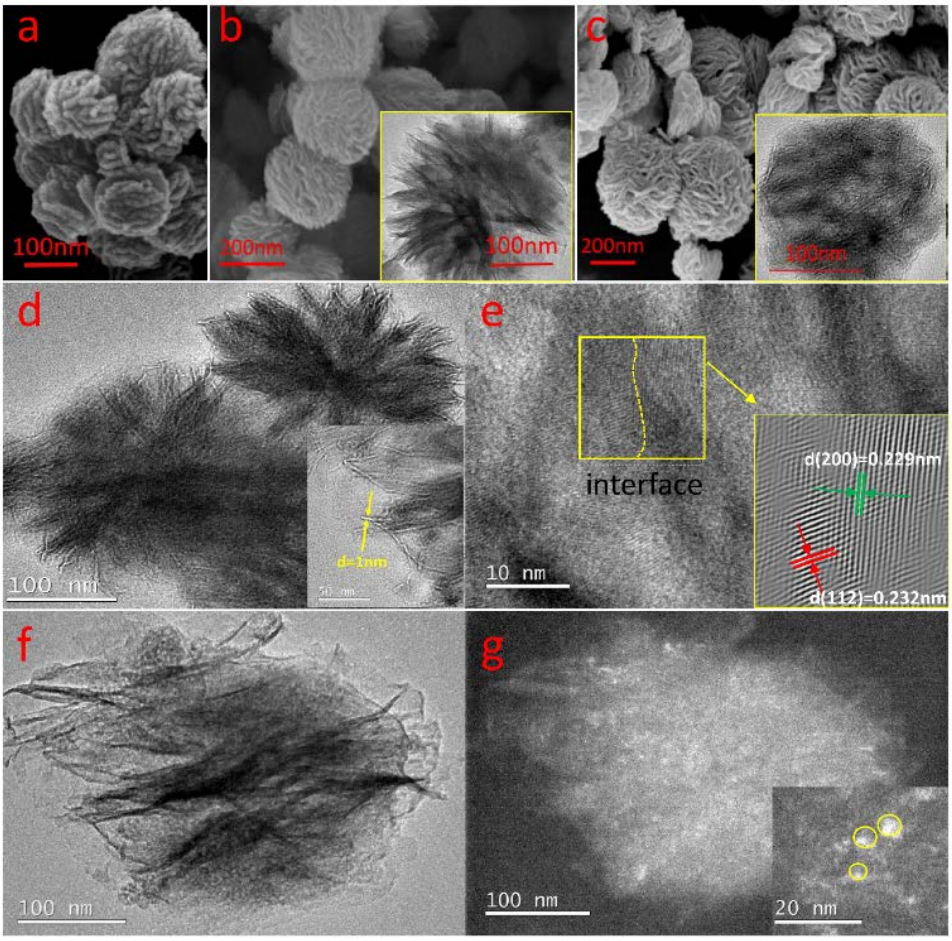

Figure 3 Electron microscope characterizations. SEM images of as-prepared (a) hydrothermal tubular TiO_2, (b) sheet TiO_2 and (c) TiO_2(300) annealed from tubular TiO_2. The insets in (b) and (c) are the corresponding TEM images of one sphere. TEM characterization of TiO_2(300). (d) TEM image and high-resolution TEM image in the inset, showing thin tubes with the diameter of 1 nm. (e) Phase interface by lattice mismatch between the rutile and anatase, (200) is from rutile while (112) from anatase. (f) and (g) are the bright-field (BF) and dark-field (DF) images of the sample dispersed by sonication.

Figures 3(a) and 3(b) display the scanning electron microscopy (SEM) and transmission electron microscopy (TEM-inset) images of the TiO_2 formed by hydrothermal processing; 24 h of hydrothermal treatment results in a sphere formed from tubules, whilst 36 hours of heating yields a sphere composed of platelets. The spherical structure results from the slow hydrolysis of the

precursor that equilibrates the crystal growth kinetics in all directions and the tubular morphology arises from incomplete hydrolysis and condensation[47]. The tubules are maintained when samples hydrothermally treated for 24 h are calcined at 300 ^{o}C, see Figure 3c, but tends to collapse at the higher calcination temperature of 500 ^{o}C, leading to a decrease in surface area and the loss of nanopores (see Figure S7). Transmission electron spectroscopy (TEM) images of TiO_2(300) post sonication, Figure 3d, show that the spheres are formed of an array of nanotubes, and the high-resolution TEM, see inset, indicates that the tubes have a diameter of *ca.* 1 nm.

The selected area electron diffraction (SAED) pattern from the petals is shown in Figure S8 and the broad diffraction rings indicate the polycrystallinity of the composite, mainly assigned to anatase and rutile, which is consistent with the XRD results. An interface boundary in TiO_2(300) is shown in Figure 3e, where lattices of (112) from anatase and (200) from rutile are imaged, with a mismatch rate (δ) of 0.56 (Figure S9) denoting a rich boundary structure[14]. Both lattices have distortion and some defect areas in the lattice cross-section. The bright-field (BF) and dark-field (DF) images in Figure 3f and g indicate the aggregation of the nanoparticles along the sheets and a high concentration of aggregates that range from 1 to ~15 nm (the inset) which affect the light scattering of the material.

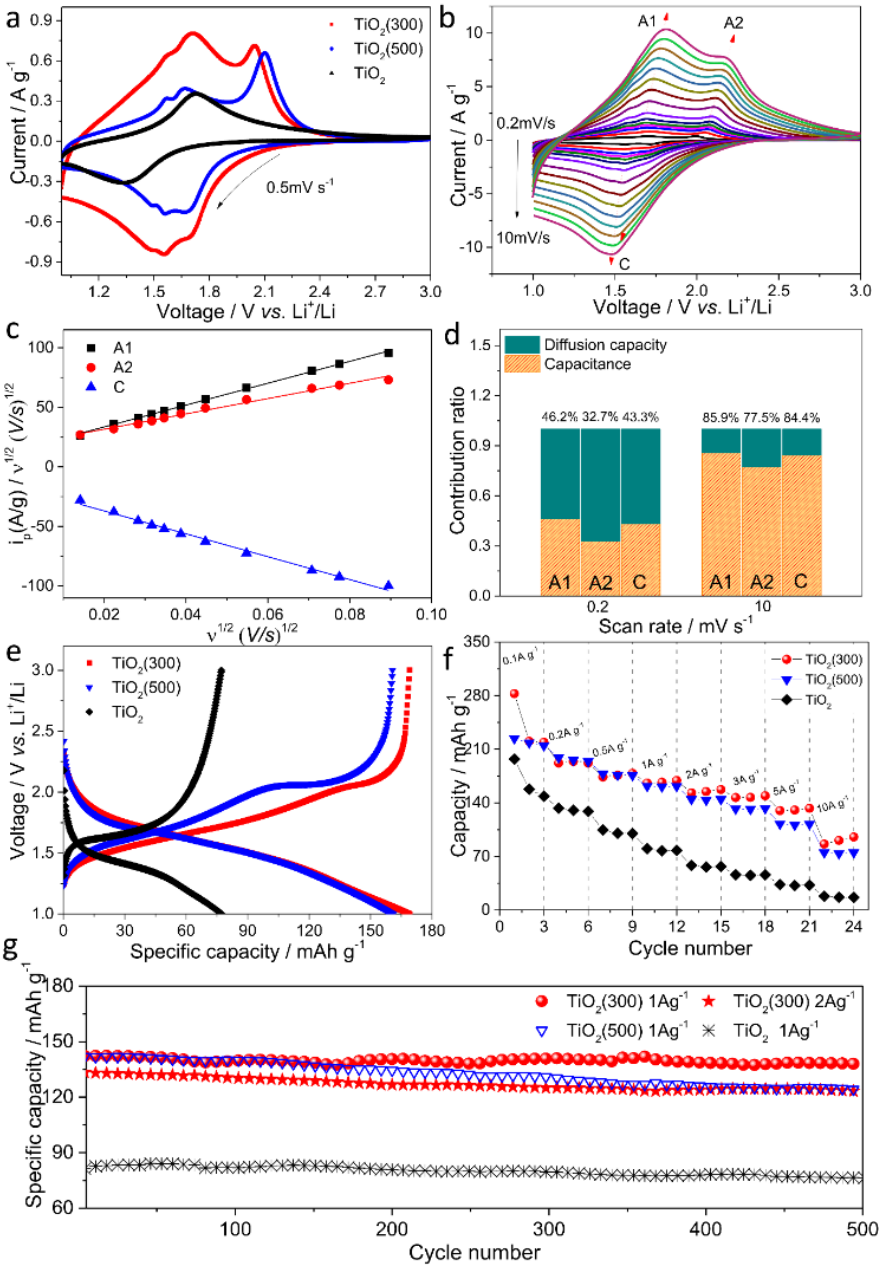

Figure 4 Electrochemical measurements on the as-prepared samples. (a) CV curves of the hydrothermal TiO_2, TiO_2(300) and TiO_2(500) at 0.5 mV s^{-1}. (b) Different scan rates related to the CV curves of TiO_2(300). (c) The kinetic analysis of the redox peaks A1, A2 and C in (b) between $i_p/v^{0.5}$ and $v^{0.5}$. (d) Ratio of the capacity contribution from diffusion and capacitance at the potential of peak current at 0.2 and 10 mV s^{-1}. (e) Galvanostatic charge-discharge profiles at a current rate of 1 A g^{-1}. (f) Rate capacity ranging from 0.1 to 10 A g^{-1}. (g) Long-term cycling stability at high rate of 1 and 2 A g^{-1}.

Typical cyclic voltammetry (CV) curves of the hydrothermal TiO_2, TiO_2(300) and TiO_2(500) recorded at a scan rate of 0.5 mV s^{-1} in the voltage range of 1 ~3 V vs. Li^+/Li are displayed in Figure 4a. The hydrothermal TiO_2 presents one pair of redox peaks at 1.7 and 1.4 V attributed to the pseudocapacitive charge storage on TiO_2-B[3]. This is consistent with the XRD results that show TiO_2-B is the dominant phase in the product of the hydrothermal reaction. Annealing at 300 °C and 500 °C increases the amount of anatase, resulting in an extra pair of peaks at 2.1 and 1.7 V for TiO_2(300) and TiO_2(500) corresponding to the incorporation of lithium ions in the bulk[10]. The broad peaks for TiO_2(300) and TiO_2(500) at potentials less than 1.7 V in the anodic and 1.6 V in cathodic are due to the overlapped current response from both rutile and TiO_2-B. Nanosized rutile has broad redox peaks between 1.5 and 2 V[12, 48, 49] and highly crystalline TiO_2-B presents split redox peaks[10], confirming the obtained rutile crystals from the hydrothermal process are nanoscale.

CVs recorded at scan rates from 0.2 to 10 mV s^{-1} were performed to investigate the kinetics of lithiation. For TiO_2(300), Figure 4b, there are two peaks, denoted A1 and A2 in anodic part of the scans. Both the anodic peaks shift to higher voltage with increasing scan rate. The shift in position of the A2 peak with scan rate is more pronounced than that of the A1 peak, reflecting the fact that the anatase phase, which gives rise to the A2 feature, is kinetically more resistive to Li^+ removal than the rutile phase. In the cathodic arm of the scans, there are two peaks at low scan rates that merge to a single peak, labelled C, at higher scan rates. Analysis of the cathodic peaks at low scan rates again shows a greater shift in peak position for the feature associated with the anatase phase than that for the rutile phase. The power law relationship, between peak current, i and scan rate, υ allows the power number (0.5 or 1) to determine a diffusion or capacitive response, according to $i=a\upsilon^b$, where a and b are adjustable parameters. Figure S10 shows *Log*(peak current) against *Log*(scan rate) and the b factor obtained denotes a complex reaction

mechanism. To quantitatively analyse the current response from each kinetic component, a combination of surface capacitance (Aυ) and diffusion intercalation (B$\upsilon^{0.5}$) is considered at each fixed potential[50]:

$$i(V) = A\upsilon + B\upsilon^{0.5} \quad (1)$$

The linear relationship between $i/\upsilon^{0.5}$ and $\upsilon^{0.5}$ is plotted in Figure 4c for all three peaks and the results depicted in Figure 4d indicate a mixed capacitive-diffusion system at 0.2 and 10 mV s^{-1} at potentials where fast Faradaic reactions occur. The capacitive contribution gradually dominates the whole capacity as the scan rate is increased from 0.2 to 10 mV s^{-1}, which is due to the small crystal size and rich capacitive area, including the surface and interface.

Galvanostatic charge-discharge profiles of the hydrothermal TiO_2, TiO_2(300) and TiO_2(500) at a current rate of 1 A g^{-1} are displayed in Figure 4e. All the S-type curves are assigned to a solid-solution intercalation/de-intercalation process without long-range ordering[9] resulting from the small crystal size and short-range order of the Ti-O octahedra. TiO_2(500) displays a longer charging plateau which is typical of "region 2" reaction of the anatase[51] in comparison with TiO_2(300), indicating the higher amount of anatase phase in TiO_2(500) and is consistent with the quantitative analysis in XRD and XPS. Figure 4e compares the rate capacity of the samples ranging from 0.1 to 10 A g^{-1} with electrode coating densities around 1 mg cm^{-2}. Both the heated samples, TiO_2(300) and TiO_2(500), show better performance than the non-annealed sample and TiO_2(300) performs outstandingly at high current rates. The specific capacity of TiO_2(300) reaches 167 mAh g^{-1} at 1 A g^{-1} (6C) and maintains 95 mAh g^{-1} at 10 A g^{-1} (60C) whilst TiO_2(500) has a specific capacity of 161 mAh g^{-1} at 1 A g^{-1} and maintains 75 mAh g^{-1} at 10 A g^{-1}. The difference in the specific capacities of TiO_2(300) and TiO_2(500) is tiny at current rates below 1 A g^{-1}. As plotted in Figure 4g, TiO_2(300) also displays superior cycling stability in comparison with the other two samples, suggesting a mixed anatase-rutile structure is beneficial. The capacity retention rate is 97.2% at 1 A g^{-1} and 92.7% at 2 A g^{-1} after 500 cycles.

Furthermore, in contrast with the other published work, listed in Table 2, the synthesized TiO_2(300) exhibits extraordinary performance in both rate capability and cycling stability. At lower loadings of active electrode material on the copper substrate, e.g., 0.5 and 0.3 mg cm^{-2}, even higher rate capabilities of TiO_2(300) are observed, see Figure S11.

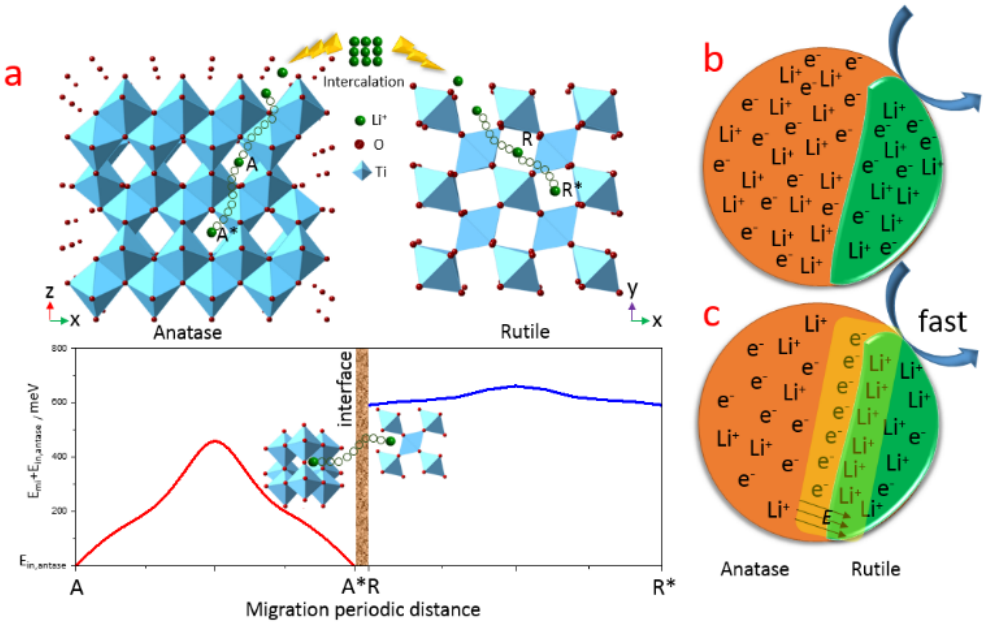

Figure 5 Representation of the anatase and rutile phase for lithium ion intercalation. (a) Schematic graph of lithium ion intercalation and migration in anatase and rutile phases, and the energy for lithium ion intercalation and migration in a periodic unit distance of each phase. $E_{in,\ anatase}$ signifies the energy for lithium ion intercalating and E_{mi} means the migration energy needed along the periodic pathway. (b) Equilibrium Li^+ ion and electron conduction in mixed anatase/rutile. (c) Synergistic transport of Li^+ ions and electrons at high-current rates in the mixed anatase/rutile with formed dobule layer structure along the interface.

To better understand the high performance of TiO_2(300) and TiO_2(500), particularly of TiO_2(300) at high charging/discharging current rates, Density Functional Theory (DFT) calculations were performed to study the ionic transport properties of the anatase and rutile. The intercalated lithium ions

prefer the O_6 octahedral sites which are energetically favourable[16] and the intercalation energy changes with the ratio of lithium ions (x) in Li_xTiO_2. Here the difference of the intercalation energy is calculated for anatase and rutile at the same intercalation ratio, and anatase shows 596 meV lower energy ($E_{in,\ anatase}$) than rutile, which is consistent with the conclusion[16] that anatase has facile Li^+ intercalation as depicted in Figure 5a. The Li^+ ion intercalation is associated with the charge transfer process between the electrolyte and electrode materials and the low energy barrier for anatase phase implies a low charge transfer resistance compared with rutile. The ability of lithium ion migration is evaluated through the migration energy which is calculated based on the lowest energy pathway for a lithium ion to move to a nearby periodic unit. Figure 5a depicts the intercalation sites and migration pathway in anatase and rutile and plots the related energy for intercalation and migration. Rutile displays a much lower energy barrier than anatase, signifying a facile transport of the of Li^+ ions.

Herein, we propose the synergistic effect between the anatase and rutile phases and on the interface to account for the high-rate performance of TiO_2(300). At low charge-discharge rates, where the voltage-drop for driving Li^+ ions through the lattice is low, the Li^+ ions and electron conductions are under equilibrium in each phase and the performance of TiO_2(300) and TiO_2(500) is very similar, suggesting both the nanosized rutile and anatase incorporate 1 mole Li per mole of TiO_2, as illustrated in Figure 5b. At higher currents, the equilibrium conduction of Li^+ ions and electrons is perturbed because the facile electron conduction in anatase and Li^+ ion conduction in rutile allow the anatase to be an electron conductor and rutile to be an ionic conductor in a high-rate reaction. The synergy of anatase and rutile is similar to the proposed "job-sharing" mechanism[52] and the existed interface can store extra capacity by forming a Li^+/e^- double layer[15], as shown in Figure 5c. The built-in electric field may facilitate the interfacial electron transfer and enhance the high-rate

performance[53]. TiO_2(300) has a high fraction of rutile with enhanced interfacial charge storage, thus performs best.

Table 2 Comparable performance in the specific capacity and cycling stability of TiO_2 as the anode in lithium-ion batteries.

TiO_2 Material	Rate Capacity / mAh g^{-1}	Cycle Stability
Degussa P25[54]	~40 (1.68 A g^{-1})	~50% (0.17 A g^{-1} over 100 cycles)
Multi-shell TiO_2 hollow sphere[54]	129 (1.68 A g^{-1})	91.9% (0.17 A g^{-1} over 100 cycles)
Anatase TiO_2 nanocages[55]	85 (1.7 A g^{-1})	~68.8% (0.17 A g^{-1} over 200 cycles)
Rutile TiO_2 submicrobox[56]	68 (4.95 A g^{-1})	96.6% (0.83 A g^{-1} over 500 cycles)
Nanosized rutile TiO_2[57]	70 (4.95 A g^{-1})	~80% (0.0083 A g^{-1} over 50 cycles)
Nanoporous anatase TiO_2[58]	151.7 (0.34 A g^{-1})	74.2% (0.17 A g^{-1} over 60 cycles)
Anatase hollow TiO_2 microbox[59]	63 (3.4 A g^{-1})	96.9% (0.17 A g^{-1} over 300 cycles)
Hollow TiO_2/GC sphere[60]	91 (10 A g^{-1})	92% (1 A g^{-1} over 1000 cycles)
TiO_2/MLG, anatase+TiO_2(B)[14]	35 (10 A g^{-1})	99.6% (0.1 A g^{-1} over 100 cycles)
Mesoporous TiO_2:RO_2[61]	91(10.1 A g^{-1})	89.2% (0.67 A g^{-1} over 20 cycles)
Nanoporous TiO_2[62]	77(10.1 A g^{-1})	~86.4% (1.68 A g^{-1} over 100 cycles)
Ti^{3+}- doped rutile nanorod[12]	93.6 (8.38 A g^{-1})	96.3% (0.16 A g^{-1} over 300 cycles)
Anatase/rutile (this work)	**95.4 (10 A g^{-1})**	**97.2% (1 A g^{-1} over 500 cycles)**

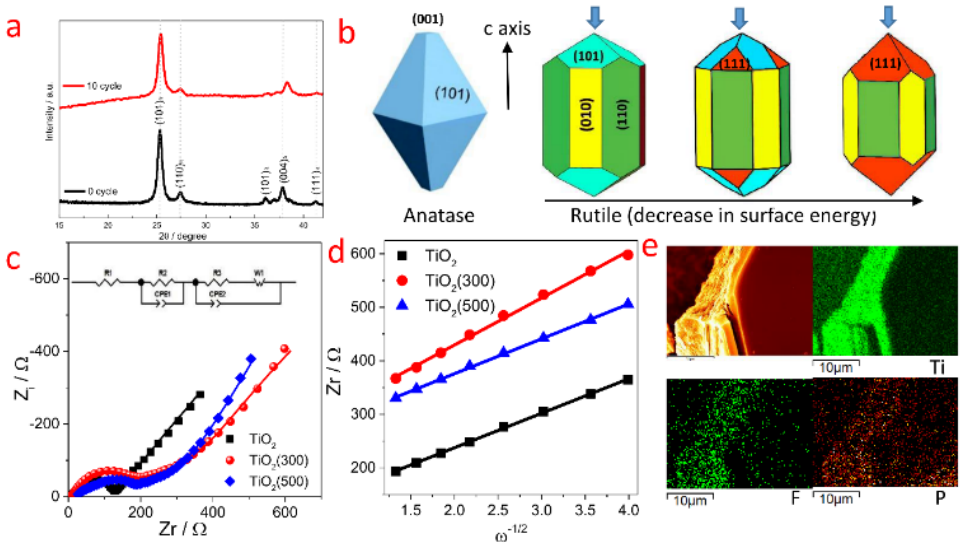

Figure 6 (a) XRD patterns of TiO_2(300) before and after 10 cycles in the lithium-ion batteries at high rate of 10 A g^{-1}. (b) Schematic representation of the thermodynamic models anatase and rutile crystals and the evolution of activated lattice plane in rutile phase upon electrochemical reaction with lithium ions (arrow). (c) Nyquist plot of the hydrothermal TiO_2, TiO_2(300) and TiO_2(500) after 500 cycles. The inset is the equivalent circuit model to fit the obtained spectra. (d) Linear relation between Z_{re} and $\omega^{-1/2}$ transformed from the Warburg region in (a). (e) Elemental mapping of the electrode after cycling from a crack area. The images displayed are SEM image, mapping of Ti, F and P.

TiO_2(300) electrode material post ten galvanostatic cycles at a current rate of 10 A g^{-1} was used to study the phase change caused by the continuous lithiation/de-lithiation. XRD patterns before and post the electrochemical reaction are displayed in Figure 6a. For both patterns, the typical diffraction peaks are fitted by using a Lorentz function and the particle sizes are obtained from Scherrer equation, as listed in Table S2. Anatase crystals show a large shrinkage along the (004) direction and rutile in the (110) and (101) directions post cycling. The thermodynamic crystal models of anatase and rutile shown in Figure 6b display the related lattice faces[63, 64]. The outmost (101) plane of anatase has the lowest surface energy and (111), (110) of rutile are the most stable planes in comparison with the others, which tend to be intercalated by lithium ions easily[64]. (101) of anatase shows an increased domain size by 2.1 nm and (110), (101) of rutile are 5.6 and 5.8 nm post cycling. The change in *d* space and domain sizes of rutile are much larger than anatase, indicating the rutile phase in the mixed-phase structure probably has larger local strain variation upon ion intercalation[65]. The (111) of rutile shows a huge variation in size by 10 nm which is due to the evolution of the activated planes by decreasing surface energy[66] in the lithium diffusion along the preferred crystallographic *c* plane[67]. The charge-discharge cycling leads to un-recovered crystallinity[68] in the lattice

and domain size for both crystals in the mixed phase with more intensive variation in rutile, resulting from the irreversible reactions in lithium uptake and release at high-rate currents.

In comparison with the reported TiO_2 of various hierarchical structures and morphologies (Table 2), TiO_2(300) displays advanced nanostructures with high surface area, resulting in short pathways for electron/Li^+ ion conduction and high contact area with the electrolyte[69, 70]; TiO_2(300) is composed of only TiO_2 polymorphs, the conductivity increase relies on the yielded defects and the improved lithium storage performance is due to the synergistic storage in the anatase/rutile composite, distinguished with other reported TiO_2 composites that use carbon materials[71-74], MXene[75] and metal oxides/sulphides[76, 77] to contribute extra buffer space, conductivity and capacity. TiO_2 has a typical cut-off voltage of 1 V vs. Li^+/Li to reduce solid electrolyte interphase (SEI) formation, and lower potentials beyond this only contribute pseudocapacitance arising from the material surface and interface[14]. The reported TiO_2 composites have to deepen the cut-off voltage to 0.01 V vs. Li^+/Li to exert extra lithium storage because of the low operation potentials of the components, *i.e.* carbon, MXene and metal oxides/sulphides. The synergy of anatase/rutile in lithium storage points out a strategy to improve the storage capacity of TiO_2 without boosting SEI formation and aiding by other high-capacity materials.

Electrochemical impedance spectroscopy (EIS) was used to study the kinetic parameters related to the TiO_2/Li half-cell system. Figure 6c displays the Nyquist plots, recorded at a dc potential of 1.3 V *vs.* Li^+/Li, for electrodes formed from the hydrothermal TiO_2, TiO_2(300) and TiO_2(500) after 500 cycles. An equivalent circuit is shown in the inset of Figure 6c, and corresponding lines of best fit for each material are plotted and the associated values for each component are listed in Table S3. In the equivalent circuit, R1 represents the series resistance of the cell, that mainly arises from the electrode and electrolyte, R2 and CPE1 (constant phase element) are related to the surface resistance and capacitance,

which can be attributed to the porous electrode or SEI film on the electrode surface[15], R3 represents the charge transfer resistance, W1 is the Warburg resistance resulting from the solid-state ion diffusion in the electrode channels and CPE2 is the pseudocapacitance that is generated on the complex surface of internal boundaries[15]. According to Table S2, the capacitance of CPE2 of TiO_2(300) is much larger than for the other two. This may be due to additional charge storage at the interface between the anatase and rutile phases; such interfacial charge storage has been reported for systems containing anatase-TiO_2(B) junctions[14, 15]. The charge transfer resistance, R3 of TiO_2(500) is slightly lower than TiO_2(300) because of the high ratio of anatase in TiO_2(500) leading to low intercalation energy and high conductivity, evidenced from the DFT and EPR results. The ion diffusion which influences the rate-capability of the electrode[78] can be determined through the Warburg region in Figure 6c. The linear relation between Z_{re} and $\omega^{-1/2}$ (where ω is the angular frequency) in the low-frequency excitation range (Figure 6d) gives the Warburg factor, σ according to the following equation:

$$Z_{re}=R+\sigma\omega^{-1/2} \quad (2)$$

The ion diffusion coefficient (D) is calculated from the reported equation[51]:

$$D=\frac{1}{2}\left[\left(\frac{V_m}{FS\sigma}\right)\left(\frac{dE}{dx}\right)\right]^2 \quad (3)$$

where V_m is the molar volume, F the Faraday constant, S is the effective contact area between electrode and electrolyte, (dE/dx) is the slope of the electrode potential E vs. composition x (see Figure S12). The calculated ion diffusion coefficients are 1.1×10^{-11}, 3.3×10^{-12} and 8×10^{-12} $cm^2\ s^{-1}$ for the hydrothermal TiO_2, TiO_2(300) and TiO_2(500). The results are in good agreement with the reported conclusion and DFT analysis in this work. The hydrothermal TiO_2 mainly composed of TiO_2(B) which possesses the pseudocapacitive charging mechanism exhibit facile electrochemical diffusibility[79] and the smaller ionic diffusivity of TiO_2(300) compared with TiO_2(500) indicates a rich phase boundary in TiO_2(300) which causes high activation energy of the overall

diffusion at low frequencies[80]. Figure 6e displays the SEM image and elemental mapping of Ti, F and P of the electrode post cycles from a crack area. The non-correlated distribution of F and P in the mapping of the electrode surface and cross section denotes the electrolyte decomposition and formation of SEI film.

Experimental

Synthesis of TiO_2: All the chemicals were purchased from Sigma-Aldrich and used without any further processing. In the preparation route, 3.1 mL $TiCl_3$ solution (~10 wt. % in 20-30 wt. % hydrochloric acid) was mixed with 94 mL ethylene glycol (anhydrous, 99.8%) by vigorous stirring for 2 h in a beaker at room temperature. Then, 3.1 mL deionized water was dropped into the solution and the stirring maintained for a further 10 min before the transfer to a 125 mL autoclave. The autoclaving reaction was performed at 150 ^{o}C in an oven for a range of reaction times (18, 24, 36 h). The obtained hydrothermal products were then calcinated in air at temperatures of 300 and 500 ^{o}C for 2 h with a heating rate of 2 ^{o}C min^{-1}.

Material Characterization: The crystallographic structure of the as-prepared materials was studied by X-ray powder diffraction (XRD) using a Bruker D8 diffractometer with monochromatic Cu Kα radiation (λ = 1.5406 Å), and the diffraction data was recorded in the 2θ range of 10–80 ^{o}. Scanning electron microscopy (SEM) images were recorded on an LEO Gemini 1525 FEG. Transmission electron microscopy (TEM) images, selected area electron diffraction (SAED) were carried out on JEM 2100F. X-ray photoelectron spectroscopy (XPS) was measured using a Thermo Scientific K-Alpha instrument. The thermogravimetric analysis/differential scanning calorimetry (TGA/DSC) of the samples was carried out on a Diamond TG thermo-analyzer. Measurement of the resistivity of the materials was carried out on a Hall effect measurement system (Lake Shore, 8400 Series) using a sample pellet with 1 cm diameter that made of 150 mg material powder at a pressure of 12 tons. Ultraviolet-visible

absorption spectroscopy and diffuse reflectance spectroscopy were carried out on a Cary Series UV-Vis-NIR spectrophotometer (Agilent Technologies). Continuous wave electron paramagnetic resonance (EPR) spectra were recorded at X-band (ca. 9 GHz) on a Bruker EMX Micro spectrometer equipped with a Bruker ER4112SHQ resonator at room temperature. Samples were placed in quartz EPR tubes (4mm OD, 3mm ID) in identical quantities, placed at the same optimal position in the cavity and measured under non-saturating conditions. G values were obtained by comparison with a Bruker Strong Pitch standard (g=2.0028).

Theoretical calculation: The density functional theory (DFT) modelling of lithium intercalation and migration in crystalline TiO_2 was performed using PWSCF component with spin-polarized Generalized Gradient Approximation (GGA+U) method. For anatase, a supercell with 2×2×1 (*a*×*b*×*c*) unit cells was used for intercalation calculation while for rutile, a supercell with 2×2×2 unit cells was used. A plane-wave basis with a kinetic energy cutoff of 225 Ry was used, and the optimum set of K-mesh (2×2×1) was chosen by the convergence of energy.The lattice parameters of anatase and rutile are optimized in the specific supercell before calculating the intercalation of lithium ions using DFT. For lithium intercalation in both anatase and rutile TiO_2, a hight ratio of Li/Ti of 0.0625 is assumed, and that the lithium ions prefer the intercalation at octahedral sites. In the isolated lithium migration in TiO_2, the optimized paths with lowest energy are selected along the c-axis in rutile and diagonal in anatase.

Electrochemical tests: The as-prepared electrode materials were mixed with acetylene black and binder (sodium carboxymethyl cellulose, CMC) in a weight ratio of 7:2:1 using distilled water as solvent. The solution was placed on a copper foil as the current collector and the electrode dried in a vacuum oven at 100 ^{o}C for 24 h. The R2032 coin cell was assembled in an argon-filled glove box using metallic lithium as the cathode and Celgard 2500 membrane as the

separator. The electrolyte was 1 M $LiPF_6$ dissolved in a mixture of ethylene carbonate (EC) and dimethyl carbonate (DMC) (v/v, 1/1). Cyclic voltammetry (CV) and galvanostatic charge/discharge cycling tests were carried out over a set voltage range using an Autolab workstation (GPES software) and a 580 Bycycle battery test system, respectively. Electrochemical impedance spectroscopy (EIS) was studied using a Solartron Analytical 1286 Interface and 1260 Frequency Response Analyser, an ac amplitude of 5 mV in the frequency range from 60 KHz to 10 mHz was employed. All electrochemical tests were carried out at room temperature.

Conclusions

Hierarchical TiO_2 spheres composed of ultrathin nanotubes containing anatase and rutile phases were prepared at low temperature via the control of nucleation and growth. The hydrothermal condition in the Ti^{3+} hydration affects the dendrimer structure and produces nuclei of mixed crystallography. The as-prepared TiO_2, containing 78.7% anatase and 21.3% rutile, showed superior properties in lithium storage, a specific capacity of 167 mAh g^{-1} at 1 A g^{-1} (6C) and maintained 95 mAh g^{-1} at 10 A g^{-1} (60C). The capacity retention rate was 97.2% at 1 A g^{-1} and 92.7% at 2 A g^{-1} after 500 cycles. The potential explanations for the outstanding high-rate performance of the mixed-phase anatase/rutile are: the synthesized nanostructures shorten the pathway for electron and Li^+ ion conduction; the synergistic effect between the defective anatase and rutile renders the shared conduction of electrons through the anatase and Li^+ ions *via* the rutile at high current rates; the interfacial boundaries between the two phases can contribute to extra capacitance at high rates by forming a Li^+/e^- double layer. The synergy between the anatase and rutile and interfacial storage are revealed to be beneficial for the high-kinetic reaction in lithium-ion batteries.

Conflicts of interest

There are no conflicts to declare.

Acknowledgements

We thank the President's Ph.D. Scholarship of Imperial College London, the Engineering and Physical Sciences Research Council (EPSRC, Grant: EP/L015277/1), Armourers & Brasiers Rolls-Royce Scheme Award (2018) and STFC Futures Early Career Award (2016) for financial support. The Authors acknowledge use of characterisation facilities within the Harvey Flower Electron Microscopy Suite and Ainara Aguadero's lab, Department of Materials, Imperial College London.

References

[1] X. Chen and A. Selloni, *Chem. Rev.*, 2014, 114, 9281-9282.

[2] D. L. Wood, J. Li and C. Daniel, *J. Power Sources*, 2015, 275, 234-242.

[3] Y. Tang, Y. Zhang, J. Deng, J. Wei, H. Le Tam, B. K. Chandran, Z. Dong, Z. Chen and X. Chen, *Adv. Mater.*, 2014, 26, 6111-6118.

[4] S. Liu, H. Jia, L. Han, J. Wang, P. Gao, D. Xu, J. Yang and S. Che, *Adv. Mater.*, 2012, 24, 3201-3204.

[5] D. Deng, *Energy Sci. Eng.*, 2015, 3, 385-418.

[6] M. Wagemaker, W. J. H. Borghols and F. M. Mulder, *J. Am. Chem. Soc.*, 2007, 129, 4323-4327.

[7] W. J. H. Borghols, M. Wagemaker, U. Lafont, E. M. Kelder and F. M. Mulder, *Chem. Mater.*, 2008, 20, 2949-2955.

[8] A. R. Armstrong, C. Arrouvel, V. Gentili, S. C. Parker, M. S. Islam and P. G. Bruce, *Chem. Mater.*, 2010, 22, 6426-6432.

[9] S. Patra, C. Davoisne, H. Bouyanfif, D. Foix and F. Sauvage, *Sci. Rep.*, 2015, 5, 10928.

[10] Y. Cai, H. E. Wang, S. Zhuan Huang, J. Jin, C. Wang, Y. Yu, Y. Li and B. L. Su, *Sci. Rep.*, 2015, 5, 11557.

[11] A. R. Armstrong, G. Armstrong, J. Canales and P. G. Bruce, *Angew. Chem., Int. Ed.*, 2004, 43, 2286-2288.

[12] J. Chen, W. Song, H. Hou, Y. Zhang, M. Jing, X. Jia and X. Ji, *Adv. Funct. Mater.*, 2015, 25, 6793-6801.

[13] T. Beuvier, M. Richard-Plouet, M. Mancini-Le Granvalet, T. Brousse, O. Crosnier and L. Brohan, *Inorg. Chem.*, 2010, 49, 8457-8464.

[14] W. Song, J. Chen, X. Ji, X. Zhang, F. Xie and D. J. Riley, *J. Mater. Chem. A*, 2016, 4, 8762-8768.

[15] Q. L. Wu, J. G. Xu, X. F. Yang, F. Q. Lu, S. M. He, J. L. Yang, H. J. Fan and M. M. Wu, *Adv. Energy Mater.*, 2015, 5, 1401756.

[16] J. A. Dawson and J. Robertson, *J. Phys. Chem. C*, 2016, 120, 22910-22917.

[17] M. L. Sushko, K. M. Rosso and J. Liu, *J. Phys. Chem. C*, 2010, 114, 20277-20283.

[18] W. Zhou, L. Gai, P. Hu, J. Cui, X. Liu, D. Wang, G. Li, H. Jiang, D. Liu, H. Liu and J. Wang, *CrystEngComm*, 2011, 13, 6643.

[19] Y. Lei, J. Sun, H. Liu, X. Cheng, F. Chen and Z. Liu, *Nanoscale*, 2014, 6, 14237-14243.

[20] Y. Lei, J. Li, Z. Wang, J. Sun, F. Chen, H. Liu, X. Ma and Z. Liu, *Nanoscale*, 2017, 9, 4601-4609.

[21] D. Yang, H. Liu, Z. Zheng, Y. Yuan, J.-c. Zhao, E. R. Waclawik, X. Ke and H. Zhu, *J. Am. Chem. Soc.*, 2009, 131, 17885-17893.

[22] D. O. Scanlon, C. W. Dunnill, J. Buckeridge, S. A. Shevlin, A. J. Logsdail, S. M. Woodley, C. R. A. Catlow, M. J. Powell, R. G. Palgrave, I. P. Parkin, G. W. Watson, T. W. Keal, P. Sherwood, A. Walsh and A. A. Sokol, *Nat. Mater.*, 2013, 12, 798-801.

[23] V. D. Hildenbrand, H. Fuess, G. Pfaff and P. Reynders, *Zeitschrift für Physikalische Chemie*, 1996, 194, 139-150.

[24] G. Li, L. Li, J. Boerio-Goates and B. F. Woodfield, *J. Mater. Res.*, 2011, 18, 2664-2669.

[25] J. E. D. Davies and D. A. Long, *J. Chem. Soc. A*, 1968, DOI: 10.1039/J19680002560, 2560-2564.

[26] S. Cassaignon, M. Koelsch and J.-P. Jolivet, *J. Phys. Chem. Solids*, 2007, 68, 695-700.

[27] S. T. Aruna, S. Tirosh and A. Zaban, *J. Mater. Chem.*, 2000, 10, 2388-2391.

[28] N. Satoh, T. Nakashima, K. Kamikura and K. Yamamoto, *Nat. Nanotech.*, 2008, 3, 106-111.

[29] N. Satoh, T. Nakashima and K. Yamamoto, *Sci. Rep.*, 2013, 3, 1959.

[30] D. A. H. Hanaor and C. C. Sorrell, *J. Mater. Sci.*, 2010, 46, 855-874.

[31] K. Yanagisawa and J. Ovenstone, *J. Phys. Chem. B*, 1999, 103, 7781-7787.

[32] J. F. Banfield, D. R. Veblen and D. J. Smith, *Am. Mineral.*, 1991, 76, 343-353.

[33] J. F. Banfield and D. R. Veblen, *Am. Mineral.*, 1992, 77, 545-557.

[34] J. S. Kang, J. Lim, W.-Y. Rho, J. Kim, D.-S. Moon, J. Jeong, D. Jung, J.-W. Choi, J.-K. Lee and Y.-E. Sung, *Sci. Rep.*, 2016, 6, 30829.

[35] E. Gharibshahi and E. Saion, *Int. J. Mol. Sci.*, 2012, 13, 14723-14741.

[36] B. P. Pichon, C. Leuvrey, D. Ihiawakrim, D. Tichit and C. Gérardin, *J. Phys. Chem. C*, 2011, 115, 23695-23703.

[37] Y. Xu, S. Wu, P. Wan, J. Sun and Z. D. Hood, *RSC. Adv.*, 2017, 7, 32461-32467.

[38] W. Fu, G. Li, Y. Wang, S. Zeng, Z. Yan, J. Wang, S. Xin, L. Zhang, S. Wu and Z. Zhang, *Chem. Commun.*, 2018, 54, 58-61.

[39] M. Nowak, B. Kauch and P. Szperlich, *Rev. Sci. Instrum.*, 2009, 80, 046107.

[40] M. Wajid Shah, Y. Zhu, X. Fan, J. Zhao, Y. Li, S. Asim and C. Wang, *Sci. Rep.*, 2015, 5, 15804.

[41] C. P. Kumar, N. O. Gopal, T. C. Wang, M.-S. Wong and S. C. Ke, *The Journal of Physical Chemistry B*, 2006, 110, 5223-5229.

[42] X. Pan, M.-Q. Yang, X. Fu, N. Zhang and Y.-J. Xu, *Nanoscale*, 2013, 5, 3601-3614.

[43] J. Chen, Z. Ding, C. Wang, H. Hou, Y. Zhang, C. Wang, G. Zou and X. Ji, *ACS Appl. Mater. Interfaces*, 2016, 8, 9142-9151.

[44] Y. Zhang, Z. Ding, C. W. Foster, C. E. Banks, X. Qiu and X. Ji, *Adv. Funct. Mater.*, 2017, 27, 1700856.

[45] S. K. Misra, S. I. Andronenko, D. Tipikin, J. H. Freed, V. Somani and O. Prakash, *J. Magn. Magn. Mater.*, 2016, 401, 495-505.

[46] P. Deák, B. Aradi and T. Frauenheim, *Phys. Rev. B*, 2012, 86, 195206.

[47] P. D. Cozzoli, A. Kornowski and H. Weller, *J. Am. Chem. Soc.*, 2003, 125, 14539-14548.

[48] P. Kubiak, M. Pfanzelt, J. Geserick, U. Hörmann, N. Hüsing, U. Kaiser and M. Wohlfahrt-Mehrens, *J. Power Sources*, 2009, 194, 1099-1104.

[49] M. G. Choi, Y.-G. Lee, S.-W. Song and K. M. Kim, *Electrochim. Acta*, 2010, 55, 5975-5983.

[50] J. Wang, J. Polleux, J. Lim and B. Dunn, *J. Phys. Chem. C*, 2007, 111, 14925-14931.

[51] W. Song, X. Ji, Z. Wu, Y. Zhu, Y. Yao, K. Huangfu, Q. Chen and C. E. Banks, *J. Mater. Chem. A*, 2014, 2, 2571-2577.

[52] J. Maier, *Nat. Mater.*, 2005, 4, 805-815.

[53] Y. Zheng, T. Zhou, C. Zhang, J. Mao, H. Liu and Z. Guo, *Angew. Chem., Int. Ed.*, 2016, 55, 3408-3413.

[54] H. Ren, R. Yu, J. Wang, Q. Jin, M. Yang, D. Mao, D. Kisailus, H. Zhao and D. Wang, *Nano Lett.*, 2014, 14, 6679-6684.

[55] Z. Wang and X. W. Lou, *Adv. Mater.*, 2012, 24, 4124-4129.

[56] X.-Y. Yu, H. B. Wu, L. Yu, F.-X. Ma and X. W. Lou, *Angew. Chem., Int. Ed.*, 2015, 54, 4001-4004.

[57] Y. S. Hu, L. Kienle, Y. G. Guo and J. Maier, *Adv. Mater.*, 2006, 18, 1421-1426.

[58] J. Ye, W. Liu, J. Cai, S. Chen, X. Zhao, H. Zhou and L. Qi, *J. Am. Chem. Soc.*, 2011, 133, 933-940.

[59] X. Gao, G. Li, Y. Xu, Z. Hong, C. Liang and Z. Lin, *Angew. Chem.*, 2015, 127, 14539-14543.

[60] H. Liu, W. Li, D. Shen, D. Zhao and G. Wang, *J. Am. Chem. Soc.*, 2015, 137, 13161-13166.

[61] Y.-G. Guo, Y.-S. Hu, W. Sigle and J. Maier, *Adv. Mater.*, 2007, 19, 2087-2091.

[62] J.-Y. Shin, D. Samuelis and J. Maier, *Adv. Funct. Mater.*, 2011, 21, 3464-3472.

[63] M. d. A. Barbosa, G. d. S. L. Fabris, M. M. Ferrer, D. H. M. d. Azevedo and J. R. Sambrano, *Materials Research*, 2017, 20, 920-925.

[64] C. L. Olson, J. Nelson and M. S. Islam, *The Journal of Physical Chemistry B*, 2006, 110, 9995-10001.

[65] R. van de Krol, A. Goossens and E. A. Meulenkamp, *J. Electrochem. Soc.*, 1999, 146, 3150-3154.

[66] A. A. Belak, Y. Wang and A. Van der Ven, *Chem. Mater.*, 2012, 24, 2894-2898.

[67] M. David, C. Elaine and O. D. Colm, *Adv. Energy Mater.*, 2017, 7, 1602291.

[68] F. Zhao, B. Wang, Y. Tang, H. Ge, Z. Huang and H. K. Liu, *J. Mater. Chem. A*, 2015, 3, 22969-22974.

[69] J. Chen, G. Zou, H. Hou, Y. Zhang, Z. Huang and X. Ji, *J. Mater. Chem. A*, 2016, 4, 12591-12601.

[70] J. Chen, Y. Zhang, G. Zou, Z. Huang, S. Li, H. Liao, J. Wang, H. Hou and X. Ji, *Small*, 2016, 12, 5554-5563.

[71] H. Xu, X.-D. Zhu, K.-N. Sun, Y.-T. Liu and X.-M. Xie, *Advanced Materials Interfaces*, 2015, 2, 1500239.

[72] L. Pan, Z.-W. Zhou, Y.-T. Liu and X.-M. Xie, *J. Mater. Chem. A*, 2018, 6, 7070-7079.

[73] L. Pan, Y. Liu, X. Xie, X. Ye and X. Zhu, *Nano Research*, 2016, 9, 2057-2069.

[74] Y. Zhang, C. W. Foster, C. E. Banks, L. Shao, H. Hou, G. Zou, J. Chen, Z. Huang and X. Ji, *Adv. Mater.*, 2016, 28, 9391-9399.

[75] Y.-T. Liu, P. Zhang, N. Sun, B. Anasori, Q.-Z. Zhu, H. Liu, Y. Gogotsi and B. Xu, *Adv. Mater.*, 2018, 30, 1707334.

[76] L. Pan, X.-D. Zhu, X.-M. Xie and Y.-T. Liu, *Adv. Funct. Mater.*, 2015, 25, 3341-3350.

[77] Z.-W. Zhou, L. Pan, Y.-T. Liu, X.-D. Zhu and X.-M. Xie, *Chem. Commun.*, 2018, 54, 4790-4793.

[78] J. Ma, C. Wang and S. Wroblewski, *J. Power Sources*, 2007, 164, 849-856.

[79] A. G. Dylla, G. Henkelman and K. J. Stevenson, *Accounts. Chem. Res.*, 2013, 46, 1104-1112.

[80] M. Wagemaker, R. van de Krol, A. P. M. Kentgens, A. A. van Well and F. M. Mulder, *J. Am. Chem. Soc.*, 2001, 123, 11454-11461.

Supporting information

Synergistic Storage of Lithium Ions in Defective Anatase/Rutile TiO_2 for High-rate Batteries

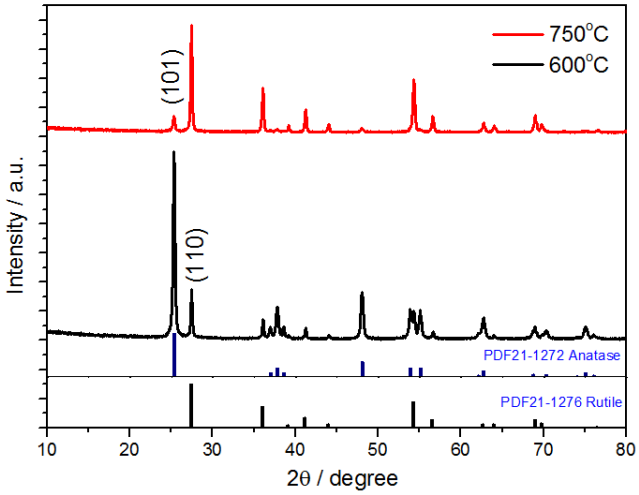

Figure S1 XRD patterns of the sintered samples from the hydrothermal TiO_2 heated in the air for 2h at 600 and 750 °C.

Table S1 Crystal size along the (101) of anatase and (110) of rutile

Temperature / °C	(101) crystal size / nm	(110) crystal size / nm
300	16.6	19.4
600	30.4	42.9
750	29.5	42.2

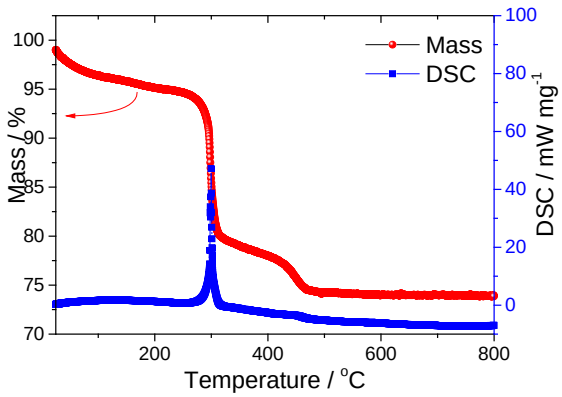

Figure S2 TG/DSC curves of the prepared TiO_2 in air with the temperature increase at 10 °C min^{-1}.

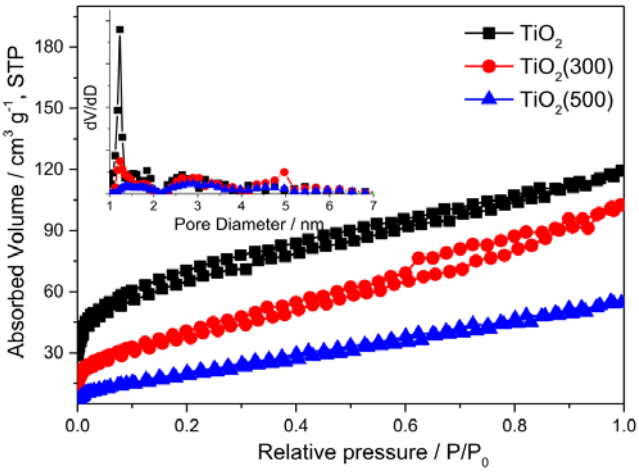

Figure S3 Nitrogen absorption/desorption curves and pore size distribution curve from the density functional theory (DFT).

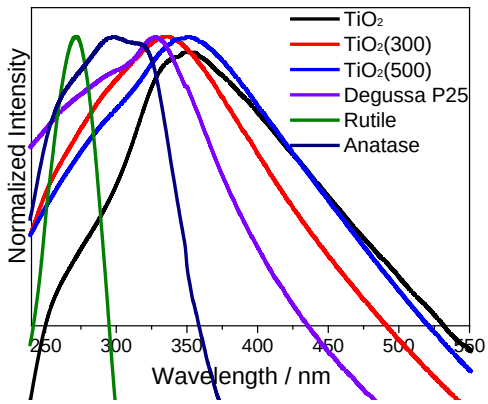

Figure S4 UV-Vis absorption spectra of the as-prepared samples in comparison with standard anatase, rutile and Degussa P25.

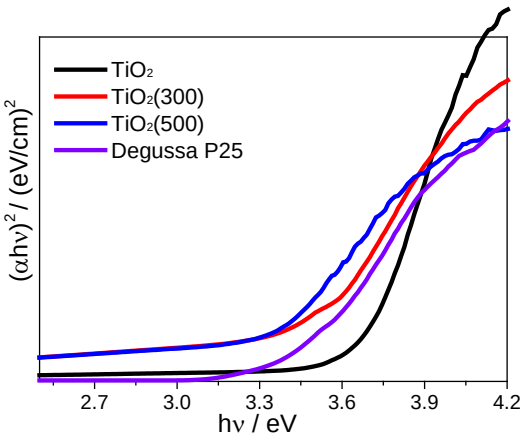

Figure S5 Tauc plots of $(\alpha h\nu)^2$ vs. photon energy ($h\nu$) for TiO_2, $TiO_2(300)$, $TiO_2(500)$ and Degussa P25.

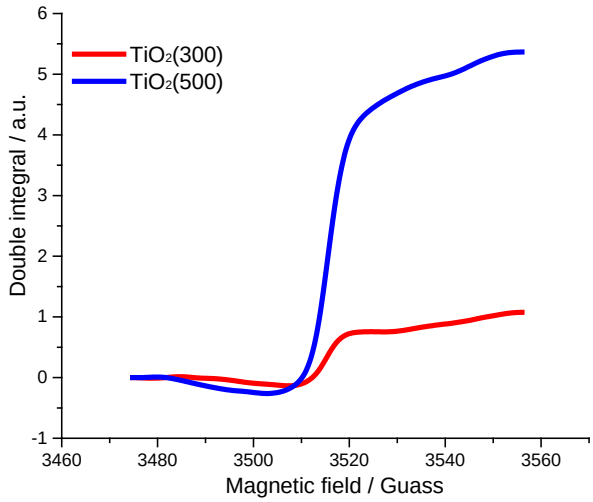

Figure S6 Doubly integrating EPR spectra of the annealed samples.

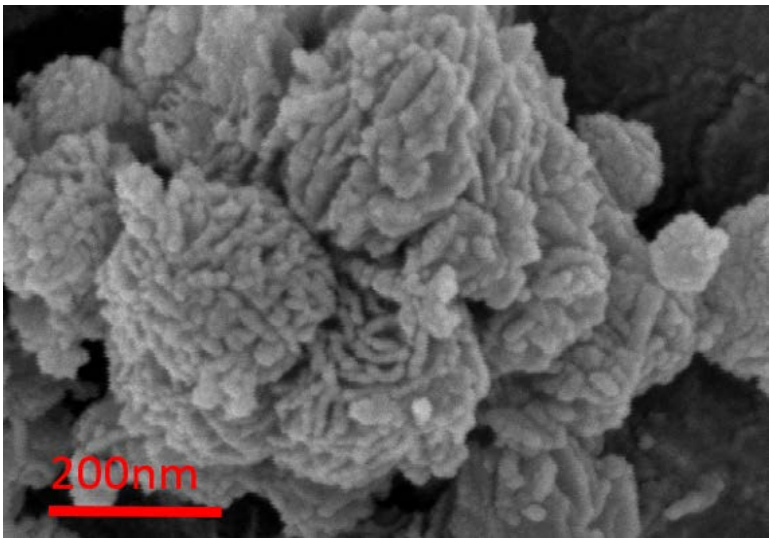

Figure S7 SEM image of TiO_2(500) annealed from tubular TiO_2.

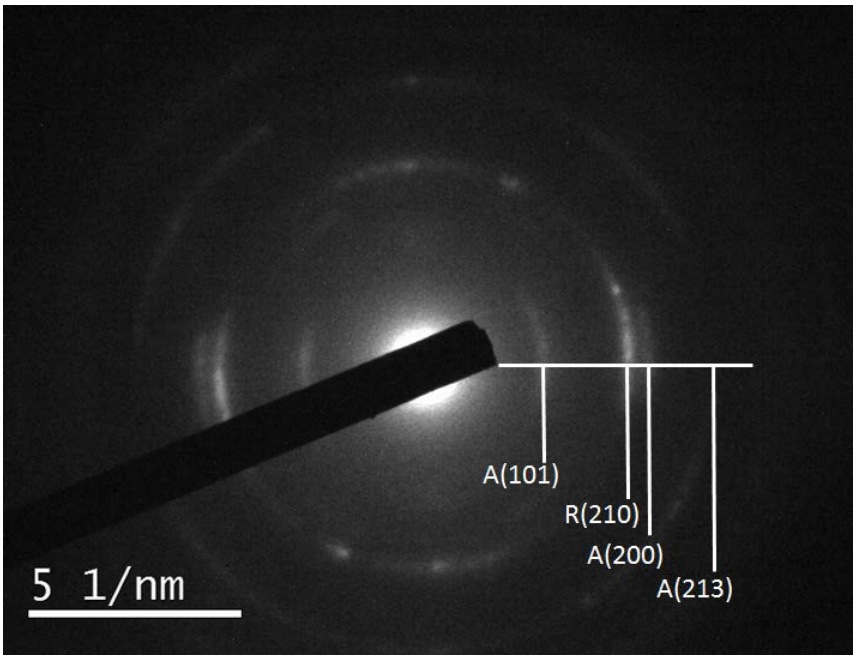

Figure S8 Selected Area Electron Diffraction (SAED) patterns from the petals shown in Figure 3(a).

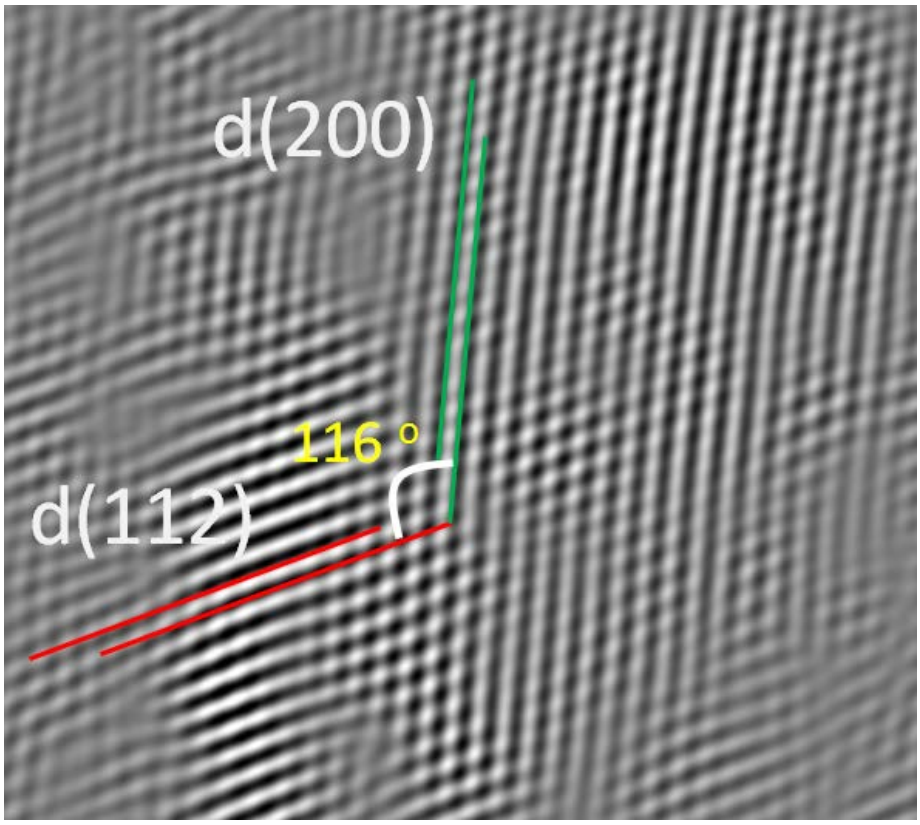

Figure S9 Lattice mismatch between the anatase and rutile phase.

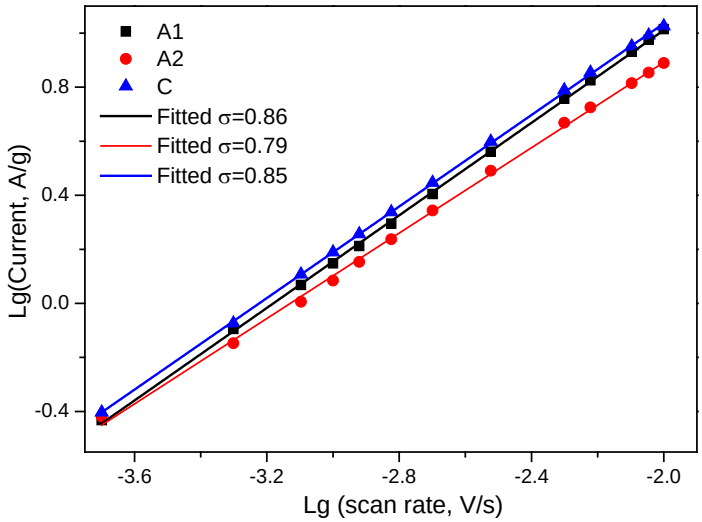

Figure S10 The linear relationship between lg(peak current) and lg(scan rate) to deduce the kinetic factor.

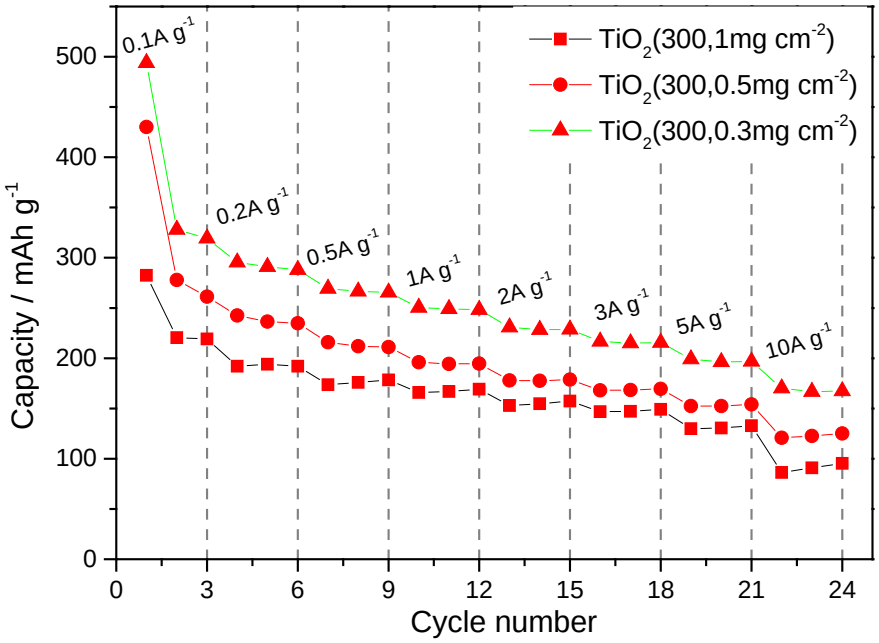

Figure S11 Rate capacity ranging from 0.1 to 10 A g^{-1} with different electrode coating density of 1, 0.5 and 0.3 mg cm^{-2}.

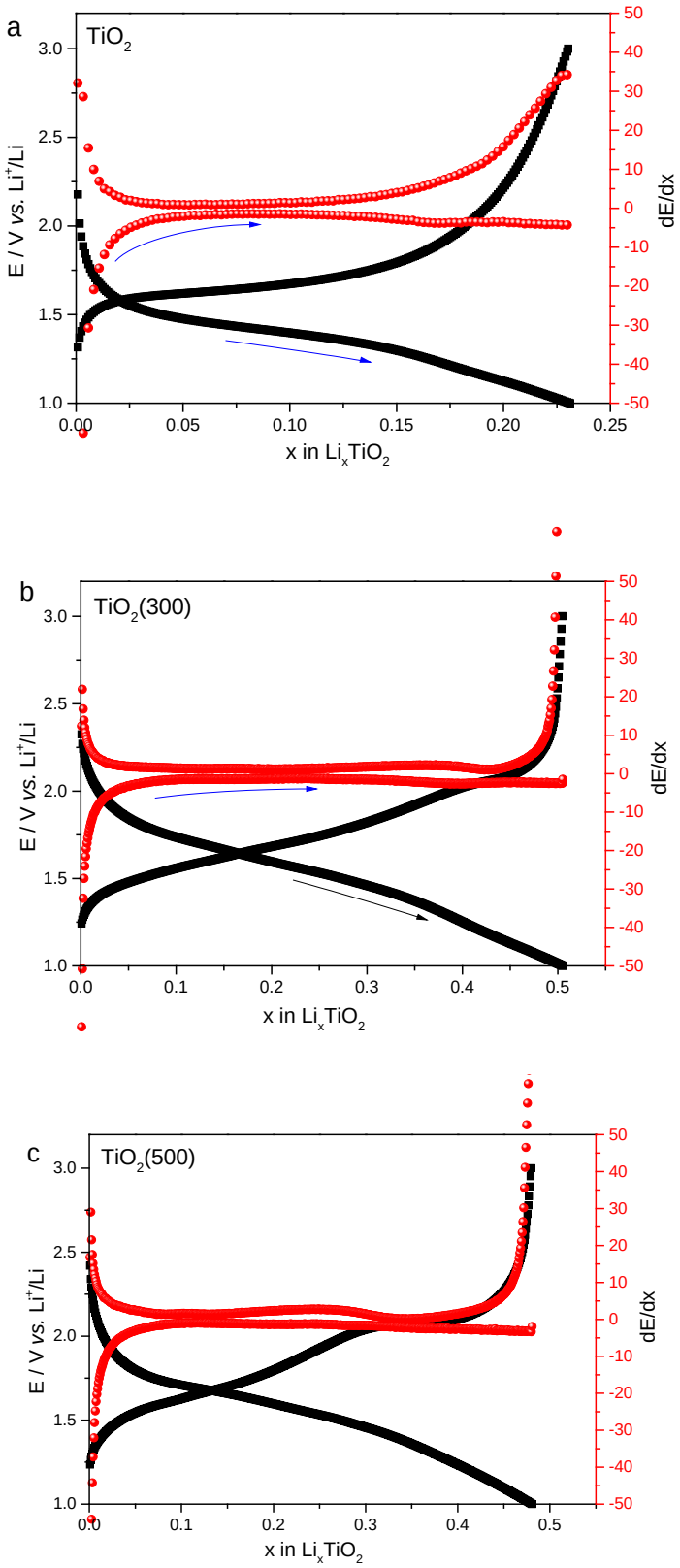

Figure S12 The relationship between dE/dx and the electrochemical potential and intercalated lithium concentration in the as-synthesized TiO_2. (a) TiO_2, (b) TiO_2(300) and (c) TiO_2(500).

Table S2 Change in lattice parameters and domain size of TiO_2 electrode before and after cycling. Diffraction peaks are fitted by Lorentz function and the particle sizes are obtained from Scherrer equation.

	0 Cycle			Post cycle		
Crystal plane	2θ/degree	d/nm	Size/nm	2θ/degree	d/nm	Size/nm
(101)A	25.27	0.352	16.4	25.36	0.351	14.3
(004)A	37.84	0.237	17.6	38.28	0.235	13.5
(110)R	27.39	0.326	17.1	27.44	0.324	11.5
(101)R	36.1	0.249	27.9	36.48	0.246	22.1
(111)R	41.19	0.219	23.9	41.36	0.218	13.9

Table S3 The value and error of each component in the equivalent circuit.

	R1/Ω	R2/Ω	CPE1/Ss^n	CPE1-P	W1/Ω	W1-T	W1-P	CPE2/Ss^n	CPE2-P	R3/Ω
TiO_2	2.85	19.34	3.4E-4	0.49	1573	209.1	0.55	3.5E-5	0.9	101.6
Error/ %	12.18	9.9	31.9	6.18	14.2	26.1	0.55	3.9	0.93	1.73
TiO_2(300)	4.9	118.8	3.7E-5	0.9	1388	11.2	0.39	0.0018	0.36	76.9
Error/ %	2.69	2.83	3.81	1.05	24.48	7.0	5.91	3.04	4.52	1.06
TiO_2(500)	20.9	78.8	6.7E-5	0.81	429.8	16.1	0.34	5.1E-5	0.6	65.52
Error/ %	1.16	4.92	4.1	1.76	1.7	3.2	0.84	11.8	1.89	6.48